



HAL
open science

The Piancaldoli meteorite: A forgotten primitive LL3.10 ordinary chondrite

Yves Marrocchi, Lydie Bonal, Jérôme Gattacceca, Laurette Piani, Pierre Beck, Richard Greenwood, Jolantha Eschrig, Anne Basque, Pasquale Mario Nuccio, Franco Foresta Martin

► To cite this version:

Yves Marrocchi, Lydie Bonal, Jérôme Gattacceca, Laurette Piani, Pierre Beck, et al.. The Piancaldoli meteorite: A forgotten primitive LL3.10 ordinary chondrite. *Meteoritics and Planetary Science*, 2020, 55 (8), pp.1924-1935. 10.1111/maps.13552. hal-03009455

HAL Id: hal-03009455

<https://hal.univ-lorraine.fr/hal-03009455v1>

Submitted on 31 Aug 2021

HAL is a multi-disciplinary open access archive for the deposit and dissemination of scientific research documents, whether they are published or not. The documents may come from teaching and research institutions in France or abroad, or from public or private research centers.

L'archive ouverte pluridisciplinaire **HAL**, est destinée au dépôt et à la diffusion de documents scientifiques de niveau recherche, publiés ou non, émanant des établissements d'enseignement et de recherche français ou étrangers, des laboratoires publics ou privés.

1 **The Piancaldoli meteorite: A forgotten primitive LL3.10 ordinary chondrite**

2
3 Yves Marrocchi^{1,*}, Lydie Bonal², Jérôme Gattacceca³, Laurette Piani¹, Pierre Beck²,
4 Richard Greenwood⁴, Jolantha Eschrig², Anne Basque¹, Pasquale Mario Nuccio⁵,
5 Franco Foresta Martin^{6,7}

6
7 ¹CRPG, CNRS, Université de Lorraine, UMR 7358, Vandoeuvre-lès-Nancy, 54501, France

8 ²Institut de Planétologie et d'Astrophysique de Grenoble, Grenoble, France

9 ³Aix-Marseille Univ, CNRS, IRD, Coll France, INRAE, CEREGE, Aix-en-Provence, France

10 ⁴PSS, Open University, Walton Hall, Milton Keynes MK7 6AA, UK

11 ⁵ Full professor of Geochemistry and Volcanology, Università di Palermo, Italy

12 ⁶Instituto Nazionale di Geofisica e Vulcanologia, Sezione di Palermo, 90146 Palermo, Italy

13 ⁷ Laboratorio Museo di Scienze della Terra, Ustica, Palermo, Italy

14
15 *Corresponding author: yvesm@crpg.cnrs-nancy.fr

26

27 **Abstract**

28 The Piancaldoli ordinary chondrite fell in northern Italy on 10 August 1968.
29 Preliminary studies led to its classification as a LL3.4 unequilibrated ordinary chondrite.
30 However, recent developments in classification procedures have prompted us to re-examine
31 its mineralogical, petrographic, spectroscopic, chemical, and isotopic features in a multi-
32 technique study. Raman spectra and magnetic properties indicate that Piancaldoli experienced
33 minimal thermal metamorphism, consistent with its high bulk hydrogen content and the Cr
34 contents of ferroan olivines in its type-II chondrules. In combination with findings of previous
35 studies, our data thus confirm the variability of Cr contents in ferroan olivines in type-II
36 chondrules as a proxy of thermal metamorphism. Furthermore, our results reveal that
37 Piancaldoli is less altered than previously reported and should be reclassified as **an** LL3.10
38 unequilibrated ordinary chondrite. Our results also imply that the bulk deuterium enrichment,
39 as observed in Piancaldoli (LL3.10), Bishunpur (LL3.15), and Semarkona (LL3.00), is a
40 specific signature of the most primitive unequilibrated ordinary chondrites. Based on our
41 results, we propose that, to date, Piancaldoli is the second least-altered unequilibrated
42 ordinary chondrite fall after Semarkona. This work reiterates the importance of meteorite
43 collections worldwide as fundamental resources for studying the formation conditions and
44 evolution our solar system.

45

46 **Keywords:** Ordinary chondrites, meteorite classification, thermal metamorphism, Piancaldoli

47

48

49

50

51 **1. Introduction**

52

53 On 26 April 1803, thousands of stones fell upon the small city of L'Aigle, France
54 (~150 km west of Paris). At that time, the extraterrestrial nature of meteorites was not yet
55 recognized and they were still considered to be ‘thunderstones’ resulting from atmospheric
56 processes. The precise description of the L'Aigle fall by dozens of people and the unique
57 nature of the recovered rocks led physicist Jean-Baptiste Biot to conclude their origin to be
58 unambiguously extraterrestrial. **The extraterrestrial origin of meteorites had already been**
59 **proposed on the basis of meteor ballistic trajectories and chemical analyses performed by**
60 **Ernst Florens Friedrich Chladni (see Marvin, 2010 for a review) and Edward Howard**
61 **(Howard et al., 1802).** Since these works, meteorites have been recognized as objects of
62 scientific importance, and natural history museums worldwide have established invaluable
63 meteorite collections. Despite the recent boom in space exploration, most of our current
64 understanding of the conditions and chronology of the formation of the solar system has been
65 established thanks to the meticulous work of meteorite collection and curation (Heck et al.
66 2019).

67 Over the past two decades, the number of meteorites reported to the Meteoritical
68 Society has increased exponentially thanks to field trips organized to cold and hot deserts
69 expressly to search for meteorites (e.g., **Harvey, 2003**; Gattacceca et al. 2011; Evatt et al.
70 2020). These harvests have enabled the characterization of some of the most primitive
71 meteorites known so far, which are now available to the scientific community. However,
72 meteorite finds are exposed to terrestrial weathering and contamination, which largely affect
73 their primitive characteristics (Alexander 2017; Stephant et al. 2018; Vacher et al. 2020). For
74 instance, Antarctic and Saharan samples are commonly affected by Na loss and/or metal
75 alteration, and Antarctic samples by oxygen isotopic exchange with Antarctic water

76 (Alexander et al. 2018). Thus, as meteorite falls are collected before any significant terrestrial
77 alteration can occur, they are of primary importance for deciphering the formation of the solar
78 system.

79 In addition to terrestrial weathering, most chondrites experienced secondary alteration
80 on their asteroidal parent bodies, resulting in changes to their primary texture, mineralogy,
81 and chemical and isotopic compositions (Brearley 2006; Marrocchi et al. 2018). These
82 petrographic and chemical modifications are the basis of petrologic type assignments (Van
83 Schmus and Wood 1967) on a scale from 1 to 6, reflecting the progressive roles of low-
84 temperature aqueous alteration (types 3 to 1) and thermal metamorphism (types 3 to 6). In
85 theory, type-3 chondrites thus correspond to primitive materials that underwent minimal
86 modifications after their agglomeration in the protoplanetary disk 4.56 Ga (Amelin et al.,
87 2010). However, new classification procedures based on thermoluminescence (TL; Sears et al.
88 1980), chemical characteristics (e.g., Cr content in ferroan olivines in type-II chondrules;
89 Grossman and Brearley 2005) and Raman spectroscopy (Bonal et al. 2006, 2007, 2016)
90 permit the quantification of discrete variations among type-3 chondrites. Accordingly, type-3
91 chondrites are now subdivided into categories ranging from 3.00 to 3.9, with 3.00 being the
92 most *primitive* extraterrestrial materials, virtually unchanged since their agglomeration in the
93 disk.

94 Because these advances in the classification of minimally altered chondrites are
95 relatively recent (Grossman and Brearley 2005; Bonal et al. 2006, 2016), many previously
96 analyzed chondrites have not been characterized according to the new classification criteria
97 nor studied in further detail after their initial classification. This is fundamental, however, as
98 the identification of primitive chondrites with minimal parent-body alteration improves our
99 understanding of the formation and evolution of solids in the protoplanetary disk. In particular,
100 Al-Mg chronology requires the characterization of refractory inclusions and chondrules in

101 chondrites of petrologic subtypes ≤ 3.1 due to the fast self-diffusion of Mg in minerals and
102 glassy mesostases (Kita and Ushikubo 2012; Van Orman et al. 2014; Marrocchi et al. 2019).

103 While vacationing in Sicily in 2018, the first author (YM) fortuitously met Franco
104 Foresta Martin, a geologist and a journalist at the Italian national daily newspaper *Corriere*
105 *della Sera*. He brought to my knowledge the history of the Piancaldoli meteorite that fell near
106 Florence in northern Italy on 10 August 1968. A fireball was observed over Yugoslavia and
107 central and northern Italy, followed by explosions accompanying the break-up of the
108 meteorite. Three meteorite fragments totaling 13.1 g were found on the roof of a house in
109 Piancaldoli. The Piancaldoli meteorite was first classified as a L3 chondrite (Carapezza and
110 Nuccio 1971) before being reclassified as LL3 (Carapezza et al. 1975, 1976). Although no
111 Raman or TL data were available for Piancaldoli, Rubin et al. (1982) proposed its
112 reclassification as petrologic type 3.4 ± 0.2 based on silicate compositions. Consequently,
113 Piancaldoli is listed as a LL3.4 ordinary chondrite in the Meteoritical Bulletin Database. Here
114 we report a comprehensive description of Piancaldoli and show that its secondary thermal
115 history was overestimated. Our results indicate that Piancaldoli is the second least-altered
116 unequilibrated ordinary chondrite fall known to date.

117

118 **2. Material and methods**

119 **2.1 Mineralogical and petrographic observations**

120 We surveyed two sections of Piancaldoli: thin section USNM 5649 from the National
121 Museum of Natural History, Smithsonian Institution (Washington D.C., USA) and a thick
122 section prepared at the Centre de Recherches Pétrographiques et Géochimiques (CRPG-
123 CNRS, Nancy, France) from a parent sample provided by the Dipartimento scienze della
124 Terra e del Mare (Palermo, Italy). We also characterized a thin section of Semarkona
125 (LL3.00; Grossman and Brearley, 2005; Muséum national d’Histoire naturelle, Paris, France)

126 and a thick section of Bishunpur (LL3.15; Grossman and Brearley, 2005; Muséum national
127 d'Histoire naturelle, Paris, France) for comparison. The sections were imaged by scanning
128 electron microscopy on a JEOL JSM-6510 equipped with a Genesis energy dispersive x-ray
129 (EDX) detector at the CRPG using a 3 nA electron beam accelerated at 15 kV. The chemical
130 compositions of olivine grains were quantified using a Cameca SXFive electron microprobe
131 at the Université Pierre et Marie Curie (UPMC, Camparis, Paris, France) using a 150 nA
132 focused beam accelerated at 15 kV. We analyzed Na, Mg, Si, Al, K, Ca, Fe, Ti, Cr, and Mn in
133 olivine grains. The high beam current allowed detection limits for silicates to be 100 ppm for
134 Al, Ca, and Ti, 150 ppm for Mn and Si, and 200 ppm for Na, K, Cr, Fe, and Mg. The PAP
135 software was used for matrix corrections.

136

137 **2.2 Raman spectroscopy**

138 Raman spectroscopy was performed at the Ecole Normale Supérieure de Lyon
139 (Laboratoire de Géologie de Lyon – Terre, Planètes, Environnement, France) using a LabRam
140 Raman spectrometer (Horiba Jobin-Yvon) equipped with a 600 gr/mm grating and a Spectra
141 Physics Ar⁺ laser ($\lambda = 514$ nm). Because carbonaceous matter is sensitive to laser-induced
142 heating and the Raman bands of polyaromatic carbonaceous matter are dispersive, we
143 followed the analytical procedures of Bonal et al. (2016, summarized here) to avoid any laser
144 alteration of the carbonaceous matter and to facilitate meaningful comparisons with reference
145 meteorites from the literature. The laser was focused through a 100× objective to obtain a ~2
146 μm spot size. The power on the sample was 500 μW . Each acquisition comprised two 30-s
147 integrations that were averaged to make the final spectrum. Spectra were acquired under
148 atmospheric conditions over the wavenumbers 500–2,200 cm^{-1} , covering the first-order
149 carbon bands. Raman spectra of carbonaceous matter in the matrix of Piancaldoli were
150 obtained both on isolated matrix fragments (50 spectra) and *in situ* in the thick section

151 prepared at the CRPG (32 spectra). Around 30 matrix fragments (typical apparent diameter
152 around 30 μm) were manually selected from a gently crushed raw piece of Piancaldoli (initial
153 sample of 50 mg) according to their color and texture under a binocular microscope. The
154 selected matrix fragments were pressed between two glass slides that served as the substrate
155 for the Raman analyses. The G and D bands were fitted with Breit-Wigner-Fano and
156 Lorentzian profiles, respectively, to retrieve spectral parameters. We compared the width (full
157 width at half maximum) of the D band ($\text{FWHM}_D, \text{cm}^{-1}$) and its intensity relative to that of the
158 G band (I_D/I_G) to those of reference samples as these spectral parameters are the most
159 sensitive to the maturity range of type-3 chondrites (e.g., Bonal et al., 2016).

160

161 **2.3 Infrared spectroscopy**

162 Infrared (IR) spectra were obtained with a Bruker HYPERION 3000 infrared
163 microscope at the Institut de Planétologie et d'Astrophysique de Grenoble (IPAG, Grenoble,
164 France). The IR beam was focused through a 15 \times objective to a typical spot size on the
165 sample of $40 \times 40 \mu\text{m}^2$. Spectra were acquired at 4 cm^{-1} spectral resolution with a MCT
166 detector cooled with liquid nitrogen. Particular care was devoted to sample preparation, which
167 is critical in IR microspectroscopy. Samples must be sufficiently thin ($<100 \mu\text{m}$) and their
168 surfaces flat and parallel to avoid absorption-band saturation and scattering artifacts,
169 respectively (Raynal et al. 2000). Small matrix fragments (30–50 μm) were selected under a
170 binocular microscope and crushed between two diamond windows for analyses in the 4000–
171 650 cm^{-1} spectral range. The diamond windows were loaded into an environmental cell,
172 designed and built at IPAG, capable of achieving temperatures up to 300 $^\circ\text{C}$ under primary or
173 secondary dynamic vacuum (10^{-4} to 10^{-7} mbar). Optical access is via both sides of the cell
174 through KBr windows, enabling measurements in transmission mode. Samples were
175 progressively heated and analyzed at 20, 100, and 300 $^\circ\text{C}$ for 1 hour at each temperature.

176 The transmission spectra were automatically converted to absorbance ($A = -\log (T/T_0)$,
177 where T_0 and T are the background and sample transmittance, respectively). To remove
178 interferences and scattering effects, a spline baseline was calculated and subtracted from the
179 raw data. The resulting spectra were normalized to the intensity of the silicate Si-O stretching
180 band (1000 cm^{-1}) at $10 \text{ }\mu\text{m}$ thickness, which does not evolve over the temperature range of
181 the measurements. Reflectance spectra were obtained on powdered fragments of Piancaldoli
182 using the SHADOWS instrument (Potin et al., 2018). Spectra were normalized to
183 spectralonTM and infragoldTM and measured under standard mode.

184

185 **2.4 Magnetic properties**

186 Hysteresis measurements were performed on a 122-mg bulk (matrix + chondrules)
187 fragment of Piancaldoli with a Princeton Micromag vibrating sample magnetometer with a
188 maximum applied field of 1 T and a sensitivity of $\sim 5 \times 10^{-9} \text{ A m}^2$. We analyzed hysteresis
189 loops to obtain the ratio of saturation remanent magnetization (M_{RS}) to saturation
190 magnetization (M_S) and the coercive force (B_C). M_S was determined by correcting the
191 hysteresis loop for the high-field susceptibility determined by a linear fit of the hysteresis
192 loops for applied fields $>0.9 \text{ T}$. Remanent coercive force (B_{CR}) was determined by back-field
193 experiments performed with the magnetometer. The coercivity spectrum was estimated from
194 the derivative of the isothermal remanent magnetization by stepwise measurements using the
195 magnetometer. The evolution of low field magnetic susceptibility at low temperature was
196 studied using an Agico MFK1 apparatus equipped with a CSL cryostat. All magnetic
197 measurements were performed at the Centre Européen de Recherche et d'Enseignement des
198 Géosciences de l'Environnement (Aix-en-Provence, France).

199

200

201 **2.5 Hydrogen isotopes**

202 Hydrogen concentrations and isotopic compositions were measured using the Thermo
203 Scientific EA IsoLink - DeltaV IRMS System at the CRPG according to the procedure
204 detailed in Lupker et al. (2012), which we summarize here. A small piece of the meteorite
205 was crushed into powder and two aliquots (5.97 and 7.82 mg, respectively) were loaded into
206 tin capsules and degassed at 120 °C under vacuum for 48 h to minimize the contribution of
207 adsorbed atmospheric water (Lupker et al. 2012; Vacher et al. 2016, 2020). Hydrogen isotopic
208 compositions are expressed relative to that of Standard Mean Ocean Water (SMOW,
209 $D/H_{SMOW} = 155.76 \times 10^{-6}$) as δD [‰] = $[(D/H_{sample} / D/H_{SMOW}) - 1] \times 1,000$.
210 Reproducibilities estimated from reference materials are better than 10% (2σ) for H
211 concentration and 0.5×10^{-6} for D/H (or 5‰ for δD).

212

213 **2.6 Oxygen isotopes**

214 High-precision oxygen isotopic measurements were performed at the Open University
215 (Milton Keynes, UK) using an infrared laser-assisted fluorination system (Miller et al., 1999;
216 Greenwood et al., 2017). Two individual analyses of whole rock chips of Piancaldoli were
217 undertaken, with each replicate having a mass of about 2 mg. After fluorination, the O₂
218 released was purified by passing through two cryogenic nitrogen traps and over a bed of
219 heated KBr. O₂ analyses were performed using a MAT 253 dual inlet mass spectrometer.
220 Analytical precision (2σ), based on replicate analyses of an internal obsidian standard, is \pm
221 0.053 ‰ for $\delta^{17}O$, \pm 0.095 ‰ for $\delta^{18}O$ and \pm 0.018 ‰ for $\Delta^{17}O$ (Starkey et al., 2016). Oxygen
222 isotopic analyses are reported in standard δ notation, where $\delta^{18}O$ has been calculated as: $\delta^{18}O$
223 = $[(^{18}O/^{16}O_{sample}/^{18}O/^{16}O_{ref.}) - 1] \times 100$ and similarly for $\delta^{17}O$ using the $^{17}O/^{16}O$ ratio. $\Delta^{17}O$,
224 which represents the deviation from the terrestrial fractionation line, has been calculated as:

225 $\Delta^{17}\text{O} = \delta^{17}\text{O} - 0.525 \times \delta^{18}\text{O}$ in order to compare our results with those obtained by Clayton et
226 al (1991).

227

228 **3. Results**

229 **3.1 Petrographic overview**

230 The Piancaldoli sections contain abundant chondrules (Figs. 1, 2) and chondrule
231 fragments (Fig. 3) in an optically dark matrix. Type-I chondrules (characterized by abundant
232 Fe-Ni metal beads, FeO-poor silicates and volatile element depletion) are predominantly
233 olivine-rich and relatively homogeneous (Fig. 2A), whereas type-II chondrule (characterized
234 by FeO-rich silicates and more chondritic abundances of volatile elements) are
235 compositionally variable with normally zoned and relict, Mg-rich, olivine grains (Villeneuve
236 et al., 2020; Fig. 2B). Some ferroan olivine grains show igneous zoning profiles, with rims
237 enriched in Cr (Fig. 4), and chromite exsolutions are commonly observed in type-II chondrule
238 olivines (Fig. 5). Although some type-II chondrules show devitrified mesostases, both types
239 are characterized by well-preserved glassy mesostases (Figs. 2–4) with no specific evidence
240 of aqueous alteration. Dusty olivine grains were observed in about 5% of 350 observed
241 chondrules. Opaque mineral assemblages are rounded and occur predominantly along
242 chondrule exteriors, but also rarely within the interiors of some chondrules (Fig. 1). Ferroan
243 olivines in type-II chondrules of Piancaldoli contain 0.2–0.5 wt.% Cr_2O_3 , averaging $0.36 \pm$
244 0.20 wt.% Cr_2O_3 (1σ , Fig. 6, Table S1); those of Semarkona and Bishunpur contain $0.45 \pm$
245 0.11 and 0.23 ± 0.13 wt.% Cr_2O_3 , respectively (Fig. 6).

246

247 **3.2 Raman and Infrared spectral characteristics**

248 Every Raman spectrum obtained of the Piancaldoli matrix exhibits the D and G bands,
249 indicating the presence of polyaromatic carbonaceous matter. We obtained mean values of

250 $\text{FWHM}_D (\text{cm}^{-1}) = 173.4 \pm 20.2$ and $I_D/I_G = 0.912 \pm 0.089$ for *in-situ* thin-section analyses ($n =$
251 32) and $\text{FWHM}_D (\text{cm}^{-1}) = 159.2 \pm 37.8$ and $I_D/I_G = 0.996 \pm 0.145$ for matrix fragments ($n =$
252 50 ; the errors reflecting the variable structural order of the polyaromatic carbonaceous matter).

253 These spectral parameters are thus variable throughout Piancaldoli: the structural order of the
254 polyaromatic carbonaceous matter in the CRPG section of Piancaldoli reflects a metamorphic
255 grade similar to that of Bishunpur (LL3.15), whereas the spectral parameters obtained for the
256 matrix fragments are more dispersed and tend to reflect a slightly higher metamorphic grade
257 (Fig. 7). This discrepancy might be explained by the brecciated nature of Piancaldoli
258 (discussed in section 4).

259 The presence of aliphatic bands in the $2800\text{--}3000 \text{ cm}^{-1}$ range of IR spectra (Fig. 8)
260 confirms our manual selection of matrix fragments because the matrix is the only
261 petrographic component containing organics in chondrites. These IR spectra mostly exhibit
262 bands related to Si-O stretching around 1000 cm^{-1} , indicating olivine to be the dominant
263 silicate. The stretching mode of molecular water is poorly visible at $\sim 3400 \text{ cm}^{-1}$, and the OH
264 band at $\sim 3670 \text{ cm}^{-1}$ is absent (Fig. 8).

265 The reflectance spectrum obtained for Piancaldoli presents the two typical absorption
266 bands at 1 and 2- μm diagnostic of Fe-bearing silicates (olivine + pyroxene). The shape bands,
267 in particular the reflectance maxima around $1.6 \mu\text{m}$, is typical of LL chondrites (Fig 9).
268 However, the depth of the two bands is lower than typical ordinary chondrites, which is likely
269 related to the unequilibrated nature of the sample. The visible reflectance at 550 nm is lower
270 than type 4-6 ordinary chondrites, and in low-side of the range of value measured for type 3
271 ordinary chondrites.

272

273

274

275 **3.3 Magnetic properties**

276 The hysteresis properties of the bulk Piancaldoli fragment are $M_S = 6.79 \text{ A m}^2/\text{kg}$, M_{RS}
277 $= 0.216 \text{ A m}^2/\text{kg}$, $B_C = 9.02 \text{ mT}$, and $B_{CR} = 62.8 \text{ mT}$, in agreement with observed values for
278 LL3 chondrite falls (Gattacceca et al. 2014). The M_S value indicates a metal content similar to
279 other LL3 chondrites. The coercivity spectrum of Piancaldoli (Fig. 10) is difficult to fit with a
280 typical combination of log-normally distributed components, and is notably shifted toward
281 low coercivities compared to other LL chondrite falls, including LL3 chondrites. In particular,
282 the absence of a peak in the high coercivity range ($>500 \text{ mT}$) precludes the presence of
283 ordered tetrataenite in cloudy zone microstructures of zoned taenite (Gattacceca et al. 2014).
284 Such microstructures form only by the cooling of Fe-Ni metal from above $320 \text{ }^\circ\text{C}$ at cooling
285 rates slower than $\sim 1000 \text{ }^\circ\text{C}/\text{Myr}$ (Gattacceca et al. 2014; Maurel et al. 2019) and can be
286 disordered by impact-induced thermal events at or above shock stage S3/S4 (Gattacceca et al.
287 2014). In the case of Piancaldoli (shock stage S1), the absence of ordered tetrataenite
288 constrains the peak metamorphism temperature to $<320 \text{ }^\circ\text{C}$. LL chondrites with broadly
289 similar coercivity spectra include Bishunpur, Krymka, and Chainpur, although Piancaldoli has
290 the lowest coercivities. Conversely, Vicencia (LL3) and all other equilibrated LL chondrites
291 have high-coercivity components attributable to ordered tetrataenite in the cloudy zone
292 structure (Fig. 10). It is therefore likely that the classification of Vicencia as LL3.2 (Keil et al.
293 2015) should be revised to a higher petrologic subtype, consistent with the observed Raman
294 spectral parameters (see their Fig. 8, and Fig. 7 herein). Indeed, Vicencia appears to be more
295 metamorphosed than Chainpur (LL3.4) and less than Tieschitz (H/L3.6).

296 **The low temperature magnetic measurements performed on Piancaldoli do not reveal a**
297 **Verwey transition at 120K that would indicate the presence of magnetite. Magnetite has been**
298 **detected through low temperature magnetic measurements in a few primitive LL3 falls, such**
299 **as Semarkona and Krymka (Keil et al., 2015), and through petrographic observation in, e.g.,**

300 Semarkona (Hutchison et al., 1987). The absence of the Verwey transition in Piancaladoli
301 confirms the absence of significant aqueous alteration.

302

303 **3.4 H and O isotopes**

304 The two analyzed aliquots of Piancaldoli contain 0.124 and 0.127 wt.% H, equivalent
305 to 1.12 and 1.14 wt.% H₂O, respectively, and have respective D/H values of 193.2×10^{-6} (δD
306 $= -57.7\text{‰}$) and 187.8×10^{-6} ($\delta D = -57.6\text{‰}$). These values are broadly typical of mildly
307 metamorphosed LL3 chondrites (Robert et al. 1979; McNaughton et al. 1982; Yang and
308 Epstein 1983; Alexander et al. 2012; Vacher et al. 2020). Although the hydrogen
309 concentrations are on the higher end of those measured for LL3 chondrites similar to
310 Semarkona (~0.04–0.12 wt.% H), the D/H ratios are intermediate among the range observed
311 for LL3 chondrites (158×10^{-6} to 505×10^{-6} ; Fig. 11).

312 The results of oxygen isotope measurement of Piancaldoli are plotted in Fig. 12. The
313 two individual analyses show consistent results with $\delta^{18}\text{O} = 5.16 \pm 0.21 \text{‰}$ (2σ) and $\delta^{17}\text{O} =$
314 $3.63 \pm 0.18 \text{‰}$ (2σ). Compared to other ordinary chondrites, Piancaldoli plots at the edge of
315 the LL chondrite field with a relatively low $\Delta^{17}\text{O}$ value of $0.95 \pm 0.08 \text{‰}$ (2σ ; Fig. 12).

316

317 **4. Discussion**

318 The Piancaldoli chondrite contains sharply defined type-I and type-II chondrules (Fig.
319 2) with a mean apparent diameter of $901 \pm 445 \text{ }\mu\text{m}$, and a median apparent diameter of $804 \text{ }\mu\text{m}$
320 ($n=352$). Rubin et al. (1982) described a Piancaldoli clast with ~100 radial-pyroxene micro-
321 chondrules 0.2–64 μm in apparent diameter. Chondrule olivine and pyroxene crystals show
322 heterogeneous compositions with (i) olivine varying between 66 and 98 mol% of forsterite
323 and (ii) pyroxene ranging from 2 to 24 mol% of ferrosilite (Carapezza et al., 1976; Rubin et
324 al., 1982). The chemical composition of Piancaldoli is typical of LL ordinary chondrites with

325 $\text{FeO}/\text{SiO}_2 = 0.48$, $\text{SiO}_2/\text{MgO} = 1.62$, and $\text{Fe}^0/\text{Fe}_{\text{tot}} = 0.12$ (Carapezza et al. 1976; Wasson and
326 Kallemeyn, 1988). In addition, the chemical compositions of the fine-grained opaque matrix
327 and the whole rock were used to propose that Piancaldoli is an unequilibrated LL ordinary
328 chondrite of petrologic type 3.4 ± 0.2 (Carapezza et al. 1976; Rubin et al. 1982). However, all
329 data collected herein indicate that Piancaldoli is more primitive than this estimation. Thus, in
330 this section, we (i) assess the extent of thermal alteration experienced by Piancaldoli and (ii)
331 propose a new classification.

332 The distribution of Cr contents in ferroan olivines in type-II chondrules is considered a
333 proxy of incipient thermal metamorphism. We obtained a mean value of 0.36 ± 0.19 wt.%
334 Cr_2O_3 (Fig. 6; Table S1) for type-II chondrule olivines in Piancaldoli, and our measurements
335 of those in Semarkona and Bishunpur during the same analytical session are in good
336 agreement with previous reports (Grossman and Brearley 2005; Fig. 6). This suggests that
337 Piancaldoli experienced minimal thermal metamorphism corresponding to petrologic type
338 3.10 (Fig. 6; Grossman and Brearley 2005), supported by the occurrence of igneous Cr zoning
339 patterns (i.e., rims enriched in Cr) in some type-II chondrule olivines (Fig. 4). Such primary
340 textures are extremely sensitive to thermal metamorphism as they are replaced by complex,
341 subparallel, needle-like exsolutions of Cr-rich phases (likely chromite; Fig. 5) upon heating
342 (Grossman and Brearley 2005). As the separation of Cr-rich phases from FeO-rich olivine
343 grains is nearly complete by petrologic type 3.2 (Grossman and Brearley 2005), the observed
344 Cr zonings in Piancaldoli olivine are a strong argument in favor of Piancaldoli's primitive
345 nature.

346 Tetrataenite dominates the magnetic properties of all but the most primitive LL
347 chondrites (and those that experienced shock stage S4 or greater). The absence of tetrataenite
348 revealed by the magnetic properties of Piancaldoli sets it among the most primitive LL
349 chondrites and constrains the peak metamorphic temperature to <320 °C. This low degree of

350 thermal metamorphism is supported by the structural order of the polyaromatic carbonaceous
351 matter in Piancaldoli. Indeed, the Raman spectral parameters of polyaromatic carbon bands of
352 Piancaldoli are comparable with those of Bishunpur (LL3.15; Fig. 7). Interestingly, spectra
353 obtained on matrix fragments selected from a piece of bulk Piancaldoli exhibit a wider
354 spectral variability, and, on average, a higher maturity (higher I_D/I_G and lower $FWHM_D$, Fig.
355 7). Therefore, some parts of Piancaldoli appear to have experienced a higher peak
356 metamorphic temperature consistent with a petrologic type closer to 3.4. This variable
357 metamorphic grade is consistent with previous petrographic observations and could be related
358 to the brecciated nature of Piancaldoli (as attested by the presence of light- and dark-colored
359 matrix domains in section USNM 5640; Rubin et al. 1982). Indeed, the fine exsolutions of Cr-
360 rich phases commonly observed in Piancaldoli (Fig. 5) suggest that it is more altered than
361 Semarkona, in which such textures are absent (Grossman and Brearley 2005).

362 Infrared spectra of Piancaldoli's matrix indicate, if not the absence, the really low
363 abundance of secondary hydrated minerals, and thus that Piancaldoli did not experience
364 significant aqueous alteration. This is in contrast to the matrix of Semarkona (LL3.00), which
365 clearly contains hydrated material, most likely smectite (Alexander et al. 1989; Quirico et al.
366 2003).

367 The hydrogen content and isotopic composition of Piancaldoli show important
368 similarities with the two least-altered ordinary chondrite falls, Semarkona and Bishunpur (Fig.
369 11). The hydrogen content of Piancaldoli (~ 0.125 wt.%) is among the highest observed in
370 ordinary chondrites (despite the removal of adsorbed atmospheric water before measurement
371 in our methodology; Vacher et al. 2016, 2020) and is similar to the highest values reported for
372 Semarkona (0.12 wt.% H; Alexander et al. 2012), further indicating that Piancaldoli
373 experienced minimal thermal metamorphism, which would have resulted in hydrogen loss
374 (Fig. 11). As neither phyllosilicates nor magnetite were observed in Piancaldoli, the H budget

375 is likely controlled by: (i) insoluble organic matter and (ii) chondrules (silicates and glassy
376 mesostases). However, a detailed TEM study should be performed to clearly rule out the
377 presence of phyllosilicates (Hutchison et al., 1987). Although enriched in deuterium
378 compared to more metamorphosed ordinary chondrites, the rather low D/H signature of
379 Piancaldoli relative to Semarkona and Bishunpur may be a consequence of the D/H
380 heterogeneities observed among unequilibrated LL chondrites. Indeed, D/H values reported
381 for Semarkona and Bishunpur are highly heterogeneous, ranging from 393 to 609×10^{-6} and
382 from 253 to 504×10^{-6} , respectively (McNaughton et al. 1982; Yang and Epstein 1983;
383 Alexander et al. 2012; Piani et al. 2015). Therefore, it seems that heterogeneous H isotopic
384 compositions can be taken as an argument for the primitive nature of unequilibrated LL
385 ordinary chondrites.

386

387

388 **5. Concluding remarks**

389 We studied the Piancaldoli chondrite via scanning electron microscopy, electron microprobe
390 analyses, hydrogen and oxygen isotopic analyses, magnetic measurements, and Raman and IR
391 spectroscopy. Characteristics of the Raman spectra and magnetic properties of Piancaldoli are
392 consistent with its primitive nature as inferred from the variability of Cr contents in ferroan
393 olivines in type-II chondrules. Furthermore, the high bulk H content of Piancaldoli indicates
394 that it experienced only minimal thermal metamorphism. Our petrographic and chemical
395 results therefore suggest that Piancaldoli should be reclassified as a LL3.10 unequilibrated
396 ordinary chondrite, rather than a LL3.4 as previously proposed. We further suggest that the
397 deuterium observed in Piancaldoli, Bishunpur, and Semarkona are specific signatures of the
398 most primitive unequilibrated LL ordinary chondrites. Our results thus demonstrate that (i)
399 Piancaldoli is the second least-altered unequilibrated ordinary chondrite fall after Semarkona,

400 and (ii) primitive meteorites are most likely sitting, unstudied, in meteorite collections
401 worldwide.

402

403

404

405

406

407

408

409

410

411

412

413

414

415

416

417

418

419

420

421

422

423

424

425 **Acknowledgments**

426 We thank Colette Guilbaud, Michel Fialin, Nicolas Rividi, Maxime Piralla, Lionel G.
427 Vacher, and Thomas Rigaudier for their assistance during sample preparation and analysis.

428 We thank Ashley King and Tim Gregory for helpful reviews and Timothy Jull for editorial
429 handling. This is CRPG-CNRS contribution #2732.

430

431

432

433

434

435

436

437

438

439

440

441

442

443

444

445

446

447

448

449

450 **Figure captions**

451

452 **Fig. 1:** Composite back-scattered electron images of Piancaldoli: (A) USNM 5649 and (B)
453 Piancaldoli-CRPG.

454

455 **Fig. 2:** Back-scattered electron images of representative (A) type-I and (B) type-II chondrules
456 with well-preserved mesostases.

457

458 **Fig. 3:** Back-scattered electron image of a fish-shaped chondrule fragment.

459

460 **Fig. 4:** EDX maps of (A) Si + Mg and (B) Cr in euhedral ferroan olivine grains in a type-II
461 chondrule of Piancaldoli. Olivine rims are enriched in Cr, representing an igneous zoning
462 profile.

463

464 **Fig. 5:** Back-scattered electron image of a ferroan olivine grain in a type-II chondrule
465 showing complex, subparallel, needle-like exsolutions of a Cr-rich phase (likely chromite).

466

467 **Fig. 6:** Standard deviation on Cr₂O₃ content *versus* mean Cr₂O₃ content of ferroan olivines in
468 type-II chondrules in Piancaldoli compared to Semarkona and Bishunpur (data from this
469 study and Grossman and Brearley, 2005). Piancaldoli lies between Semarkona and Bishunpur,
470 suggesting it is of petrologic subtype 3.10.

471

472 **Fig. 7:** Spectral parameters (FWHMD vs. ID/IG, **averages and one standard deviations**) of
473 Raman bands attributed to carbonaceous materials in Piancaldoli compared to other

474 meteorites (see Bonal et al., 2016). Data for Vicencia (LL), Axtell (CV3) and ALHA 77307
475 (CO3) are also reported (see section 3.3).

476

477 **Fig. 8:** Baseline-corrected transmission IR spectra (normalized to the height of the Si-O band
478 at 1000 cm^{-1}) of matrix fragments of Piancaldoli, acquired at $20\text{ }^{\circ}\text{C}$ under dynamic vacuum.
479 A vertical offset was applied to ease comparison. Notably, the water band is very weak and
480 olivine is the dominant silicate.

481

482 **Fig. 9:** Left: Reflectance spectra of Piancaldoli powder compared to average ordinary
483 chondrites spectra from the RELAB database. Spectra were normalized at 550 nm. Right:
484 Reflectance value at 550 nm of Piancaldoli compared to ordinary chondrites, as a function of
485 petrographic type.

486

487 **Fig. 10:** Coercivity spectra, i.e., the derivative of the isothermal remanent magnetization, IRM,
488 (normalized to saturation remanence) as a function of the acquisition field, of LL chondrite
489 falls. The petrologic types and masses of each chondrite is indicated.

490

491 **Fig. 11:** Hydrogen content (reported as $1/H_{\text{wt}\%}$) and isotopic composition of Piancaldoli
492 compared to H, L, and LL ordinary chondrites. The hydrogen concentration of Piancaldoli
493 plots in the range of poorly metamorphosed LL3 chondrites. Error bars represent 1σ standard
494 deviations for chondrites having multiply reported hydrogen compositions (data from Robert
495 et al. 1979; McNaughton et al. 1982; Yang and Epstein 1983; Alexander et al. 2012; Vacher
496 et al. 2020).

497

498 **Fig. 12:** The oxygen isotopic composition of Piancaldoli compared to H, L, and LL ordinary
499 chondrites (data from Clayton et al., 1991 and Greenwood et al., 2020) . Piancaldoli plots at
500 the edge of the LL chondrite field with a relatively low $\Delta^{17}\text{O}$ value.

501

502

503

504

505

506

507

508

509

510

511

512

513

514

515

516

517

518

519

520

521

522

523 **References**

- 524 Alexander C. M. O'D., Barber D. J., and Hutchison R. 1989. The microstructure of
525 Semarkona and Bishunpur. *Geochimica et Cosmochimica Acta* 53:3045–3057.
- 526 Alexander C. M. O'D., Bowden R., Fogel M. L., Howard K. T., Herd C. D. K., and Nittler L.
527 R. 2012. The Provenances of Asteroids, and Their Contributions to the Volatile Inventories
528 of the Terrestrial Planets. *Science* 337:721–723.
- 529 Alexander C. M. O'D. 2017. The origin of inner Solar System water. *Philosophical*
530 *Transactions of the Royal Society A: Mathematical, Physical and Engineering Sciences*
531 375:20150384–20.
- 532 Alexander C. M. O'D., McKeegan K. D., and Altwegg K. 2018. Water Reservoirs in Small
533 Planetary Bodies: Meteorites, Asteroids, and Comets. *Space Science Review* 214:36.
- 534 Amelin Y., Kaltenbach A., Iizuka T., Stirling C. H., Ireland T. R., Petaev M., Jacobsen S. B.
535 2010. U–Pb chronology of the Solar System's oldest solids with variable $^{238}\text{U}/^{235}\text{U}$. *Earth*
536 *and Planetary Science Letters* 300:343–350.
- 537 Bonal L., Quirico E., Bourot-Denise M., and Montagnac G. 2006. Determination of the
538 petrologic type of CV3 chondrites by Raman spectroscopy of included organic matter.
539 *Geochimica et Cosmochimica Acta* 70:1849–1863.
- 540 Bonal L., Bourot-Denise M., Quirico E., Montagnac G., and Lewin E. 2007. Organic matter
541 and metamorphic history of CO chondrites. *Geochimica et Cosmochimica Acta* 71:1605–
542 1623.
- 543 Bonal L., Quirico E., Flandinet L., and Montagnac G. 2016. Thermal history of type 3
544 chondrites from the Antarctic meteorite collection determined by Raman spectroscopy of
545 their polyaromatic carbonaceous matter. *Geochimica et Cosmochimica Acta* 189:312–337.

546 Brearley A. J. 2006. The action of water. In *Meteorites and the early solar system II*, edited by
547 Laurretta D. S. and McSween H. Y. Tucson, Arizona: The University of Arizona Press. pp.
548 587–624.

549 Carapezza M., and Nuccio M. 1971. The Piancaldoli meteorite. *Meteoritics* 6, 255.

550 Carapezza M., Nuccio P.M., and Valenza M. 1975. Piancaldoli meteorite: chemistry and
551 mineralogy. *Meteoritics* 10, 369.

552 Carapezza M., Nuccio P.M., and Valenza M. 1976. Piancaldoli meteorite: chemistry,
553 mineralogy and petrology. *Meteoritics* 11, 165.

554 Clayton R. N., Mayeda T. K., and Goswami J. N. 1991. Oxygen isotope studies of ordinary
555 chondrites. *Geochimica et Cosmochimica Acta* 55:2317–2337.

556 Evatt G. W., Smedley A. R. D., Joy K. H., Hunter L., Tey W. H., Abrahams I. D., and Gerrish
557 L. 2020. The spatial flux of Earth’s meteorite falls found via Antarctic data. *Geology* 48:
558 G46733.1.

559 Gattacceca J. et al. 2011. The densest meteorite collection area in hot deserts: The San Juan
560 meteorite field (Atacama Desert, Chile). *Meteoritics & Planetary Science* 46:1276–1287.

561 Gattacceca J., Suavet C., Rochette P., Weiss B.P., Winklhofer M., Uehara M., Friedrich J.
562 2014. Metal phases in ordinary chondrites: magnetic hysteresis properties and
563 implications for thermal history. *Meteoritics and Planetary Science*, 49:652-676.

564 Greenwood R.C., Burbine T.H., and Franchi I.A. 2020. Liking asteroids and meteorites to the
565 primordial planetesimals population. *Geochimica et Cosmochimica Acta* 277:377-406.

566 Grossman J. N., and Brearley A. J. 2005. The onset of metamorphism in ordinary and
567 carbonaceous chondrites. *Meteoritics & Planetary Science* 40:87–122.

568 Harvey R. 2003. The Origin and Significance of Antarctic Meteorites. *Geochemistry* 63:93-
569 147.

570 Heck P. R. et al. 2019. Best practices for the use of meteorite names in publications.
571 *Meteoritics & Planetary Science* 54:1397–1400.

572 Howard, E.C., Bournon, J.-L. Comte De, 1802. Experiments and observations on cer-
573 stony and metalline substances, which at different times are said to have fallen on the Earth.
574 *Philos. Trans. R. Soc. Lond.* 92:168–175.

575 Hutchison R., Alexander C. M. O'D., and Barber D. J. 1987. The Semarkona meteorite: first
576 occurrence of smectite in an ordinary chondrites and its implications. *Geochimica et*
577 *Cosmochimica Acta* 51:1875-1882.

578 Keil K. et al. 2015. The Vicência meteorite fall: A new unshocked (S1) weakly
579 metamorphosed (3.2) LL chondrite. *Meteoritics & Planetary Science* 50: 1089–1111.

580 Kita N. T., and Ushikubo T. 2012. Evolution of protoplanetary disk inferred from ^{26}Al
581 chronology of individual chondrules: Disk evolution and ^{26}Al chronology of chondrules.
582 *Meteoritics & Planetary Science* 47:1108–1119.

583 Lupker M. et al. 2012. Predominant floodplain over mountain weathering of Himalayan
584 sediments (Ganga basin). *Geochimica et Cosmochimica Acta* 84:410–432.

585 Marrocchi Y., Bekaert D. V., and Piani L. 2018. Origin and abundance of water in
586 carbonaceous asteroids. *Earth and Planetary Science Letters* 482:23–32.

587 Marrocchi Y., Villeneuve J., Jacquet E., Piralla M., and Chaussidon M. 2019. Rapid
588 condensation of the first Solar System solids. *Proceedings of the National Academy of*
589 *Sciences of the United States of America* 116:23461–23466.

590 Marvin U.B. 2007. Ernst Florens Friedrich Chladni (1756-1827) and the origins of modern
591 meteorite research. *Meteoritics & Planetary Science* 42:B3-B68.

592 Maurel C., Weiss B. P., Bryson J. F. J. 2019. Meteorite cloudy zone formation as a
593 quantitative indicator of paleomagnetic field intensities and cooling rates on planetesimals.
594 *Earth and Planetary Science Letters* 513:166-175.

595 McNaughton N. J., Fallick A. E., and Pillinger C. T. 1982. Deuterium enrichments in type 3
596 ordinary chondrites. *Journal of Geophysical Research* 87:A297.

597 Miller M. F., Franchi I. F., Sexton A. S. and Pillinger C. T. 1999. High precision $\delta^{17}\text{O}$
598 isotope measurements of oxygen from silicates and other oxides: methods and applications.
599 Rapid Communication in Mass Spectrometry 13:1211–1217.

600 Piani L., Robert F., and Remusat L. 2015. Micron-scale D/H heterogeneity in chondrite
601 matrices: A signature of the pristine solar system water? *Earth and Planetary Science*
602 *Letters* 415:154–164.

603 Potin S., Brissaud O., Beck P., Schmitt B., Magnard Y., Correia J.-J., Rabou P., and Jocu L.
604 2018. SHADOWS: a spectro-gonio radiometer for bidirectional reflectance studies of dark
605 meteorites and terrestrial analogs: design, calibrations, and performances on challenging
606 surfaces. *Applied Optics* 57:8279.

607 Quirico E., Raynal P.-I., Bourot-Denise M. 2003. Metamorphic grade of organic matter in six
608 unequilibrated ordinary chondrites. *Meteoritics & Planetary Science* 38:795-811.

609 Raynal P.-I., Quirico E., Borg J., Deboffle D., Dumas P., d 'Hendecourt L., Bibring J.-P., and
610 Langevin Y. 2000. Synchrotron infrared microscopy of micron-sized extraterrestrial grains.
611 *Planetary and Space Science* 48:1329–1339.

612 Robert F, Merlivat L, and Javoy M. 1979. Deuterium concentration in the early Solar System:
613 hydrogen and oxygen isotope study. *Nature* 282:785–789.

614 Rubin A. E., Scott E.R.D, and Keil K. 1982. Microchondrule-bearing clast in the Piancaldoli
615 LL3 meteorite: a new kind of type 3 chondrite and its relevance to the history of
616 chondrules. *Geochimica et Cosmochimica Acta* 46:1763–1776.

617 Sears D. W., Grossman J. N., Melcher C. L., Ross L. M., and Mills A. A. 1980. Measuring
618 metamorphic history of unequilibrated ordinary chondrites. *Nature* 287:791–795.

619 Stephant A., Garvie L. A. J., Mane P., Hervig R., and Wadhwa M. 2018. Terrestrial exposure
620 of a fresh Martian meteorite causes rapid changes in hydrogen isotopes and water
621 concentrations. *Scientific Reports* 8:12385.

622 Vacher L. G., Marrocchi Y., Verdier-Paoletti M. J., Villeneuve J., and Gounelle M. 2016.
623 Inward radial mixing of interstellar water ices in the solar protoplanetary disk. *The*
624 *Astrophysical Journal Letters* 827:1–6.

625 Vacher L.G., Piani L., Rigaudier T., Thomassin D., Florin G., Piralla M., and Marrocchi Y.
626 (2020). Hydrogen in chondrites: Influence of parent body alteration and atmospheric
627 contamination on primordial components. *Geochimica et Cosmochimica Acta* 281:53-66.

628 Van Orman J. A., Cherniak D. J., and Kita N. T. 2014. Magnesium diffusion in plagioclase:
629 Dependence on composition, and implications for thermal resetting of the ^{26}Al – ^{26}Mg early
630 solar system chronometer. *Earth and Planetary Science Letters* 385:79–88.

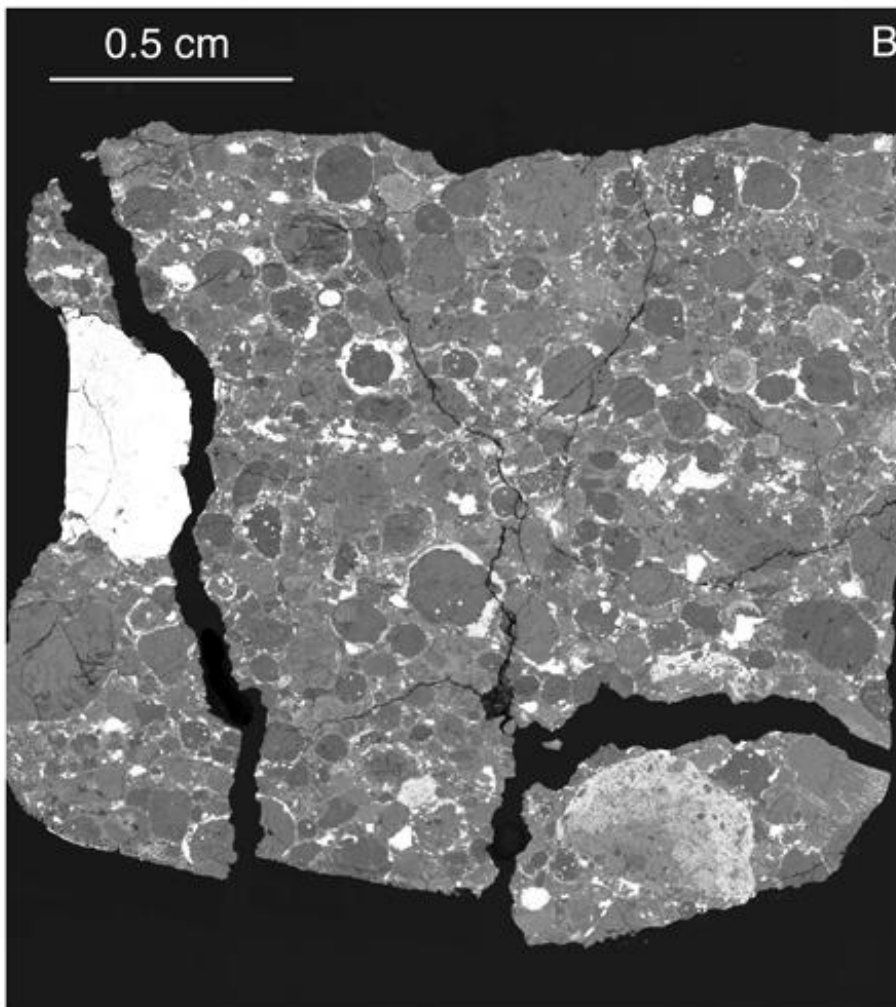
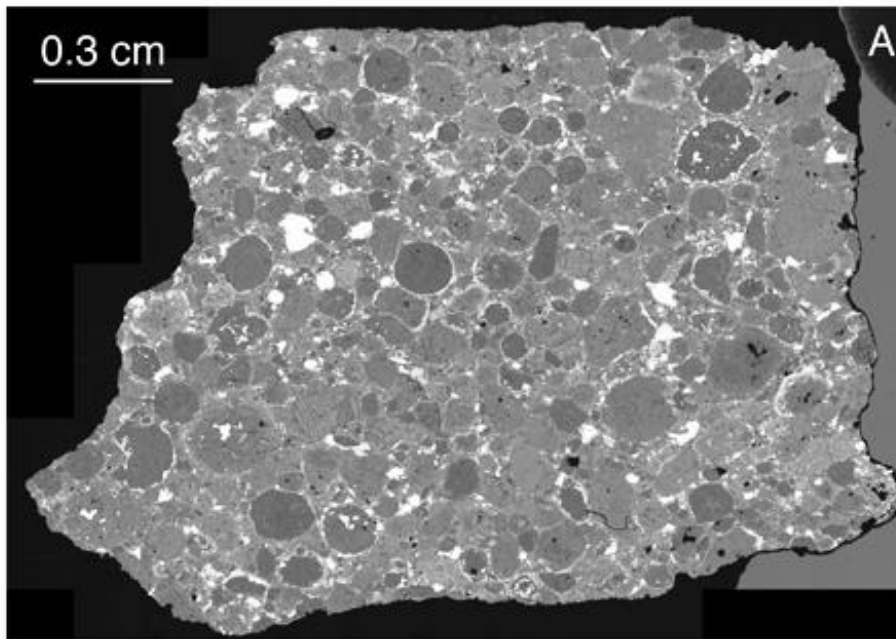
631 Van Schmus W.R., and Wood J.A. (1967) A chemical-petrologic classification for the
632 chondritic meteorites. *Geochimica et Cosmochimica Acta* 31:747-765.

633 Villeneuve J., Marrocchi Y., and Jacquet E. (2020) Silicon isotopic compositions of
634 chondrule silicates in carbonaceous chondrites and the formation of primordial solids in
635 the accretion disk. *Earth and Planetary Science Letters* 542:116318.

636 Wasson J. T., and Kallemeyn G. W. 1988. Compositions of Chondrites. *Philosophical*
637 *Transactions of the Royal Society A: Mathematical, Physical and Engineering Sciences*
638 325:535–544.

639 Yang J., and Epstein S. 1983. Interstellar organic matter in meteorites. *Geochimica et*
640 *Cosmochimica Acta* 47:2199–2216.

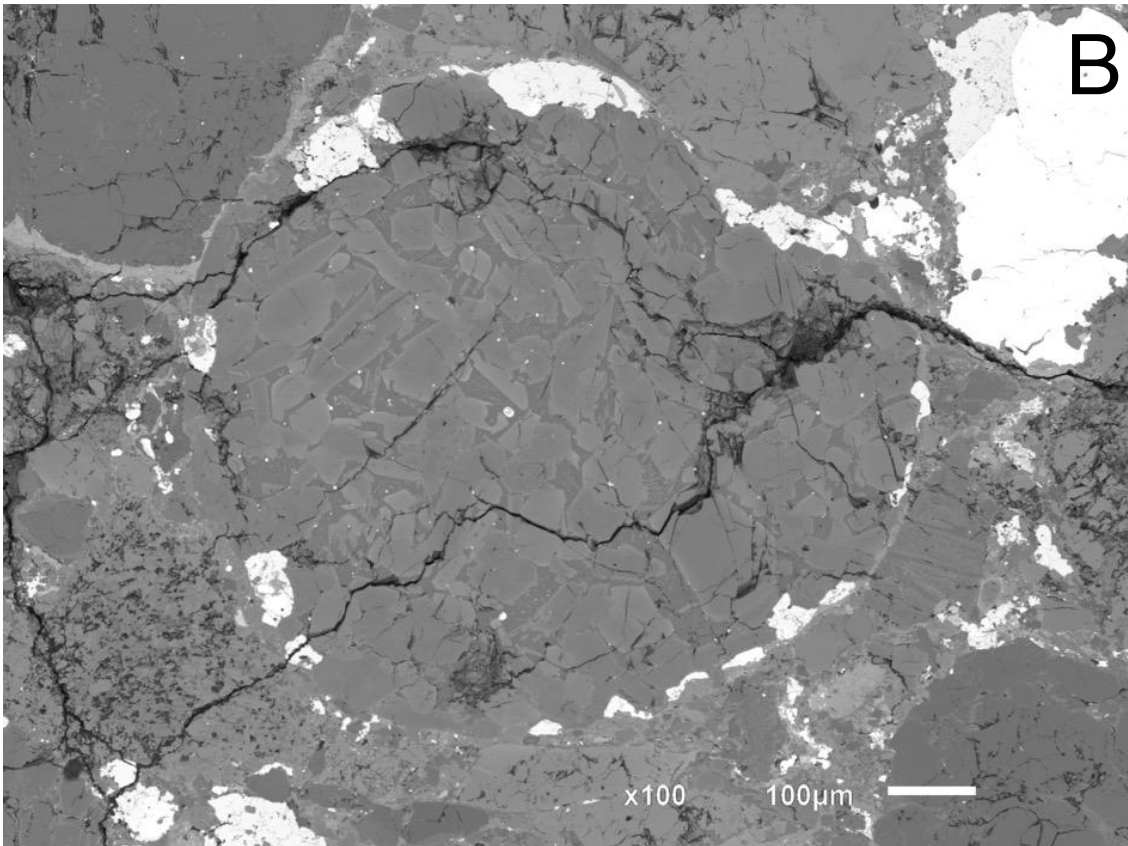
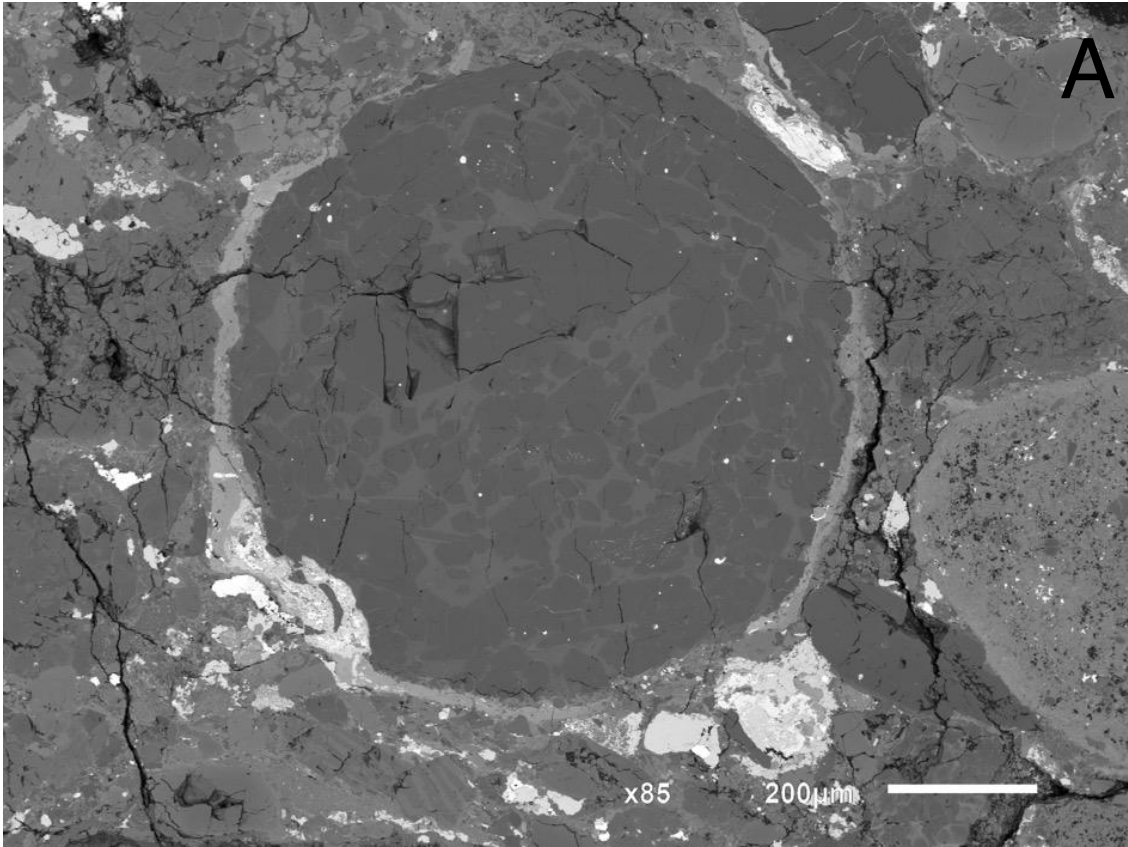
641



642

643

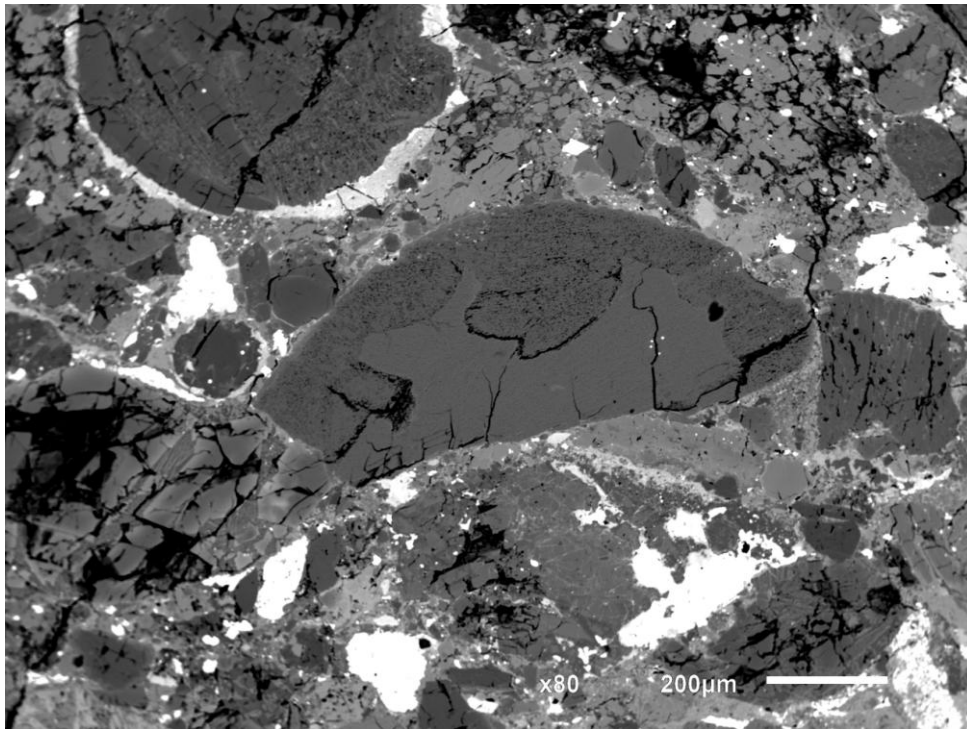
Fig. 1



644

645

Fig. 2



646

647

Fig. 3

648

649

650

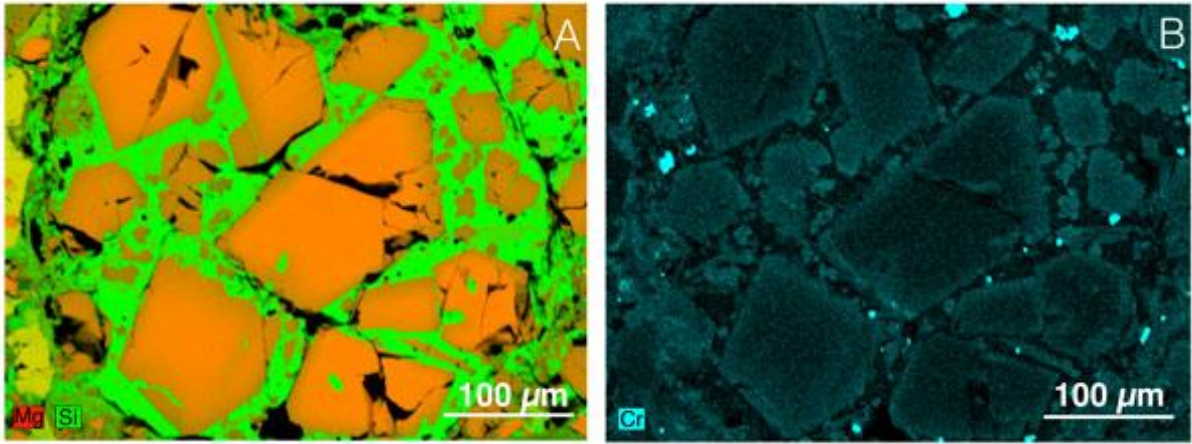
651

652

653

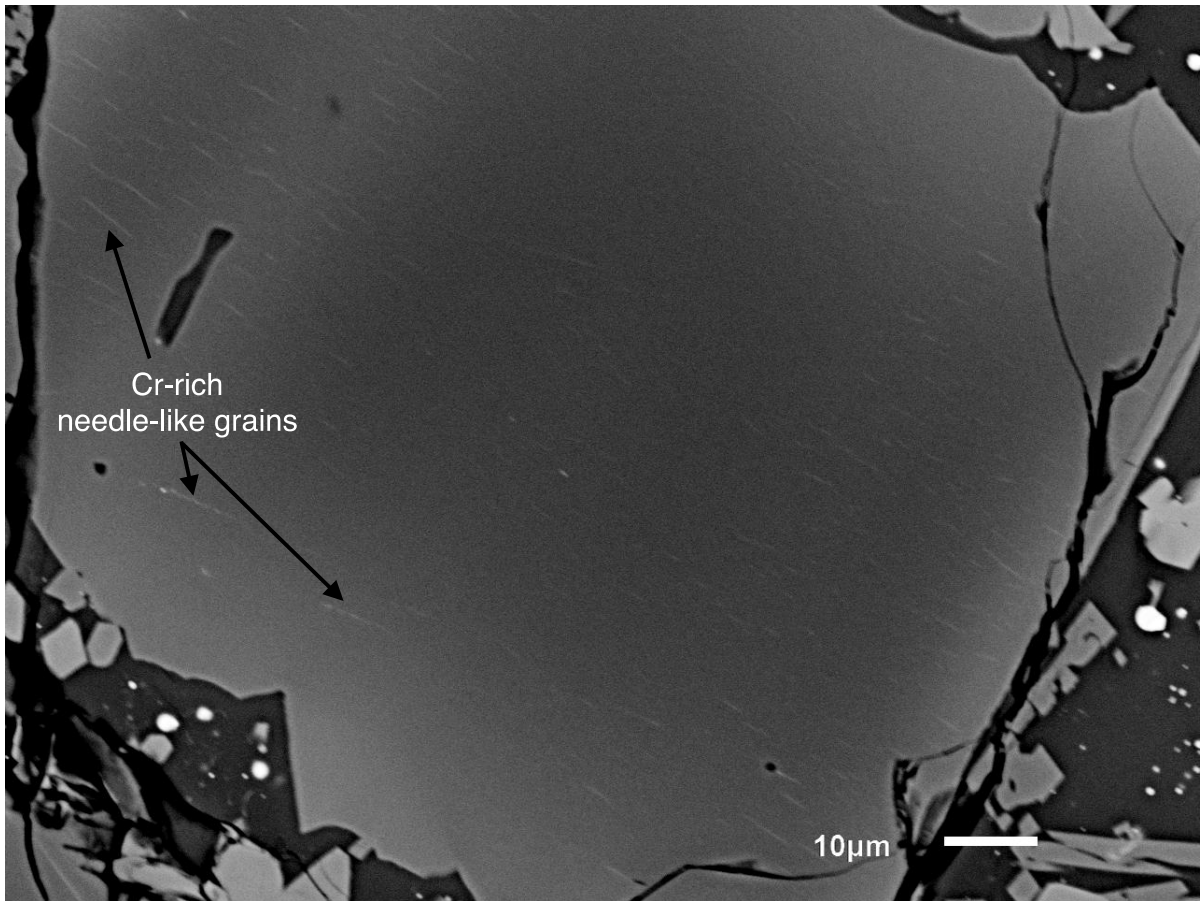
654

655



656
657
658
659
660
661
662

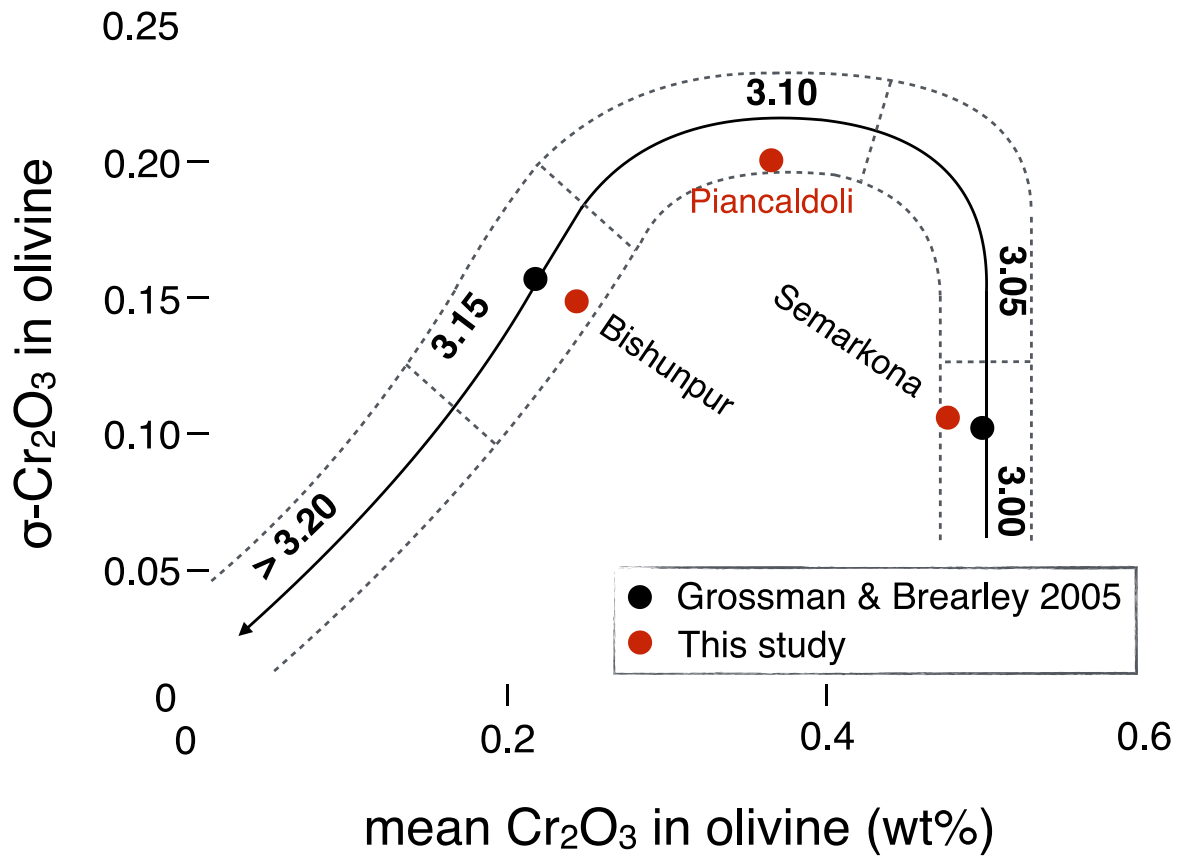
Fig. 4



663

664

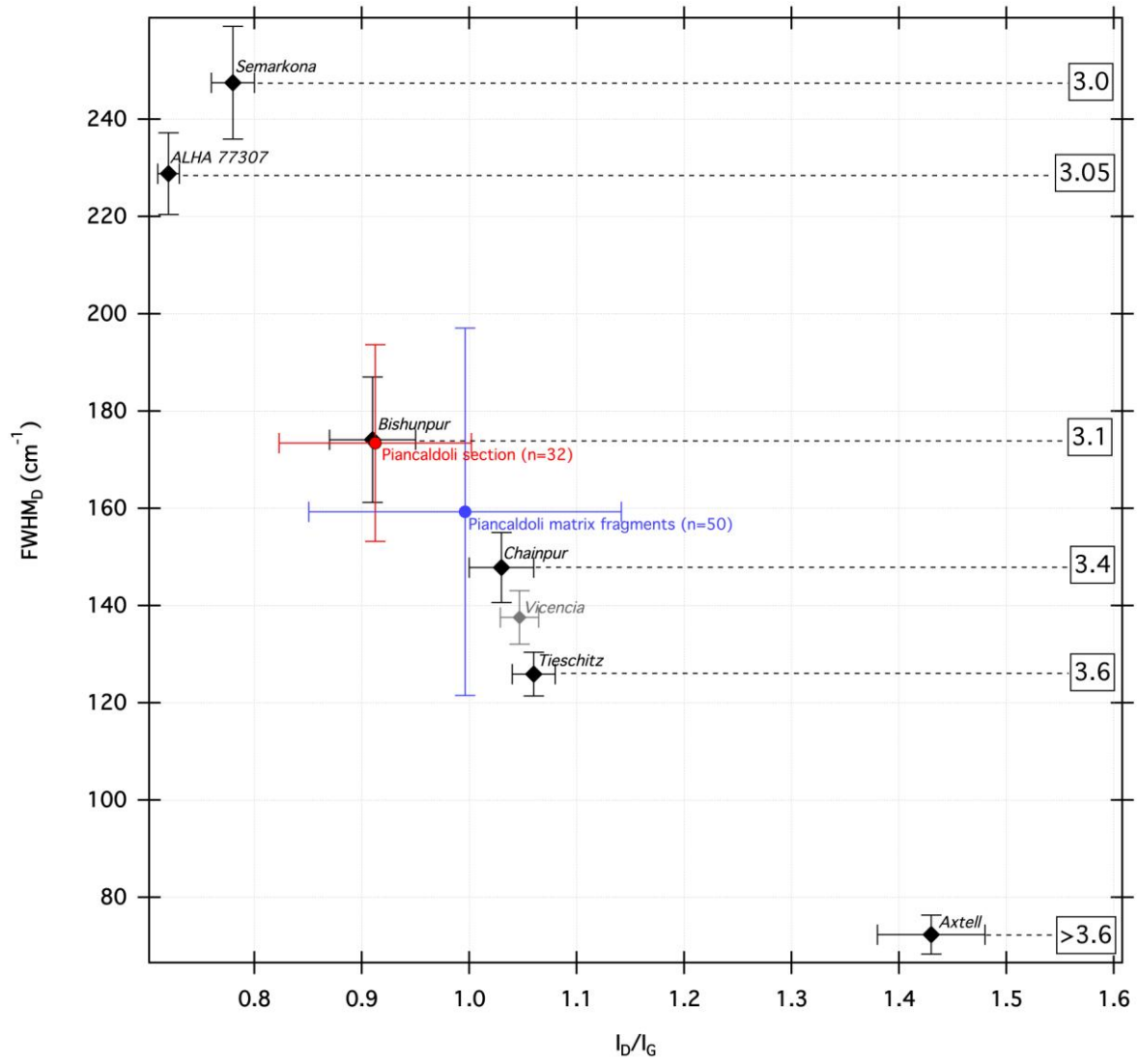
Fig. 5



665

666

Fig. 6

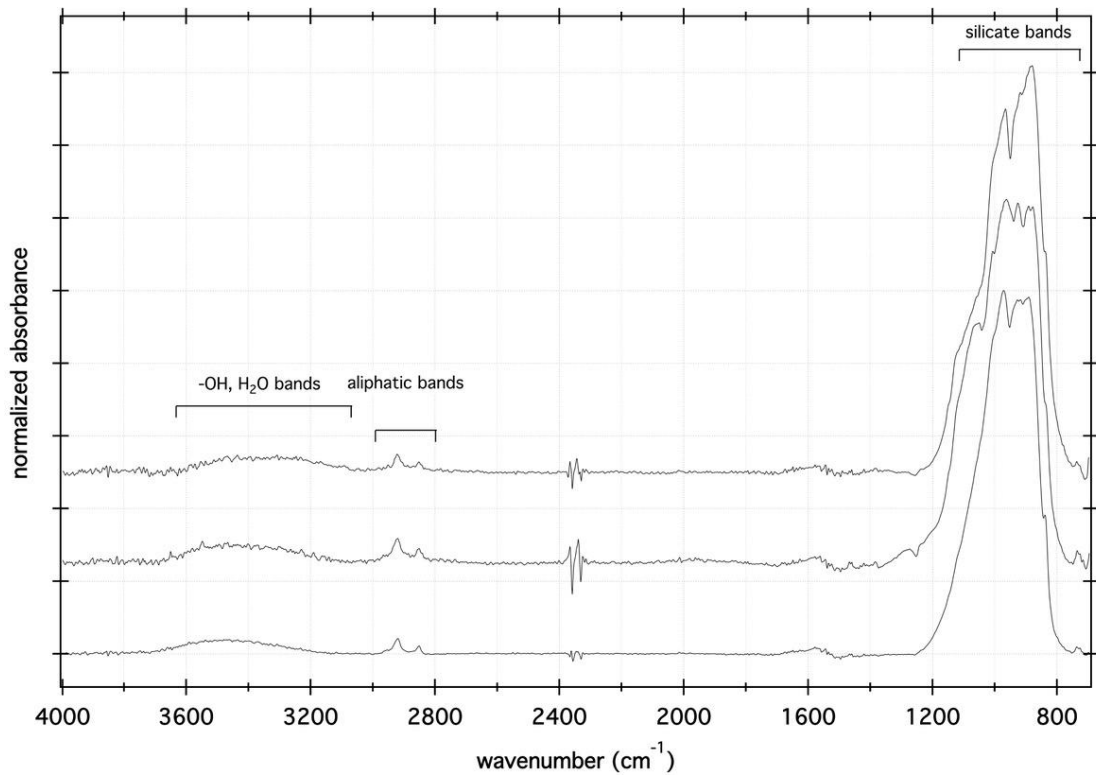


667

668

669

Fig. 7



670

671

672

673

674

675

676

677

678

679

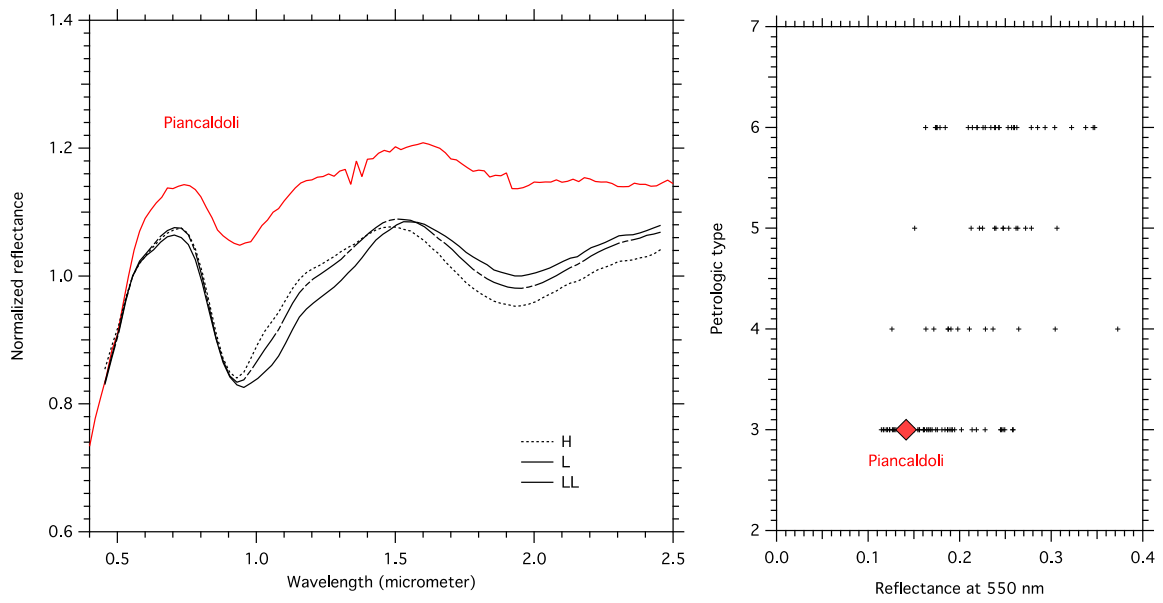
680

681

682

683

Fig. 8



684

685

686

Fig. 9

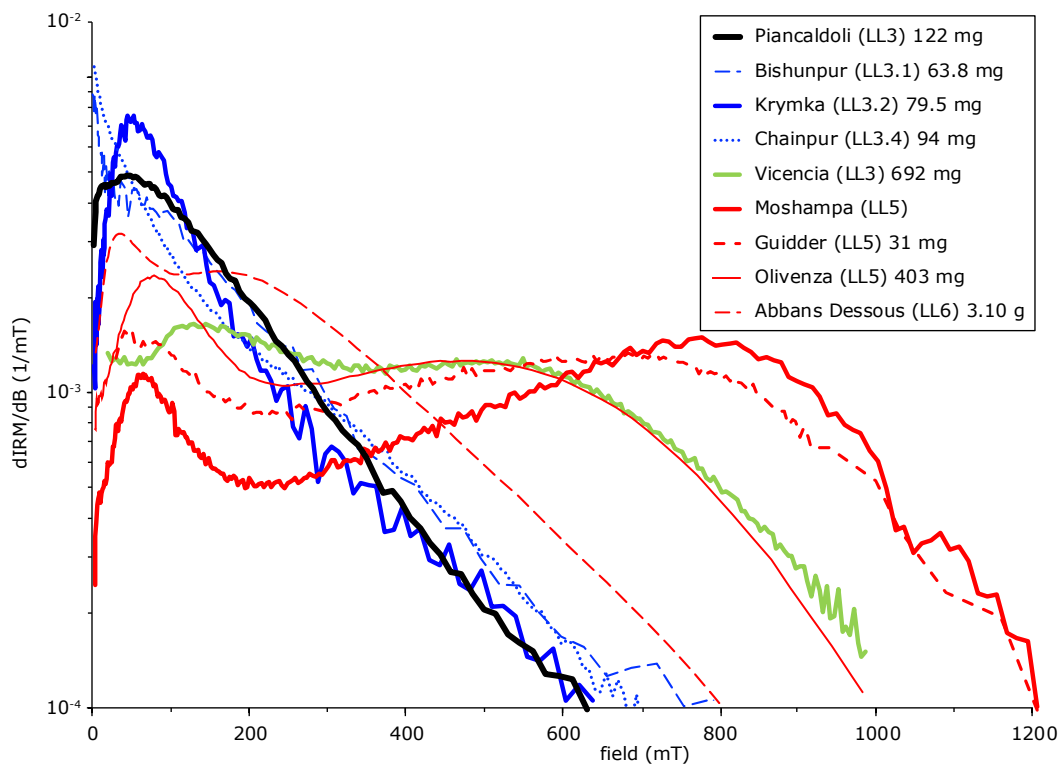
687

688

689

690

691

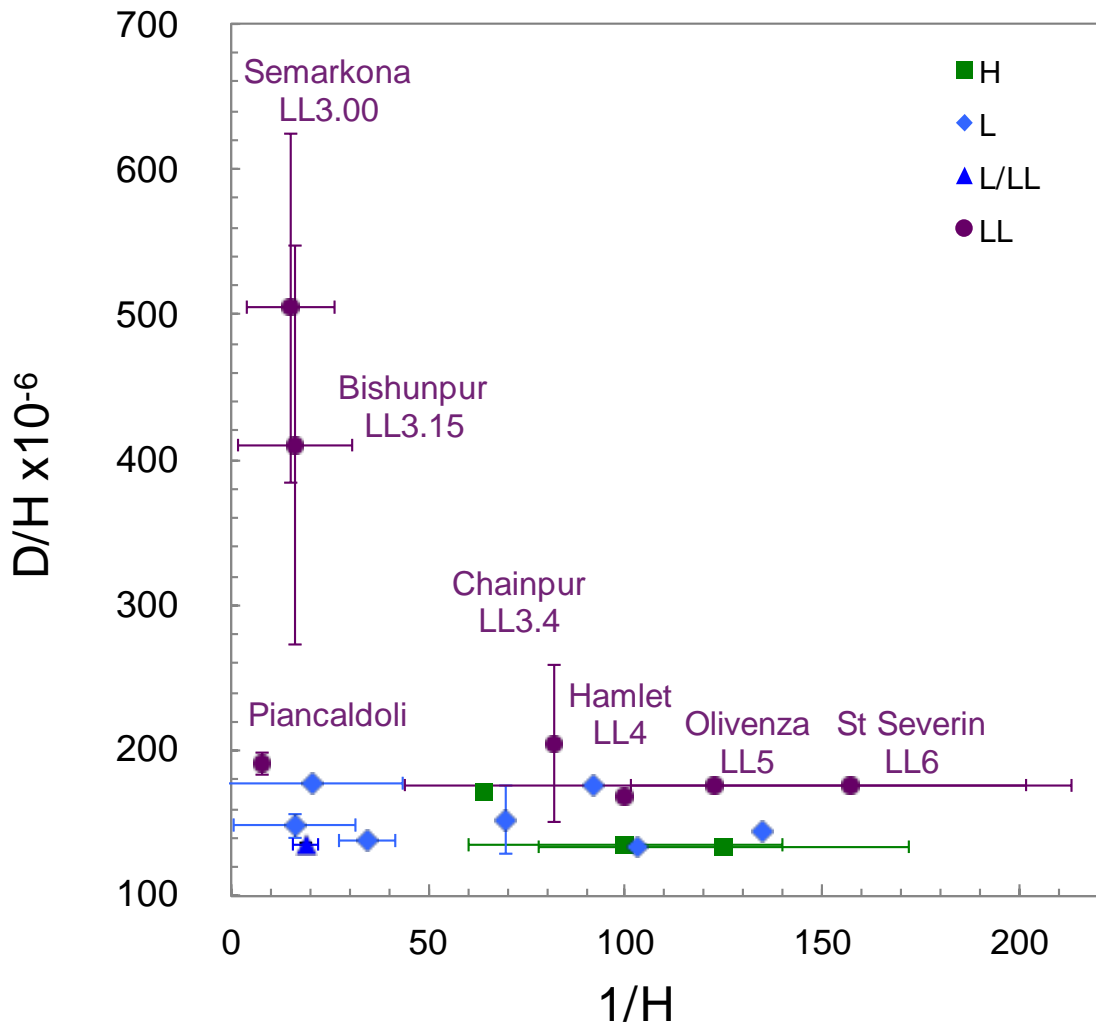


692

693

Fig. 10

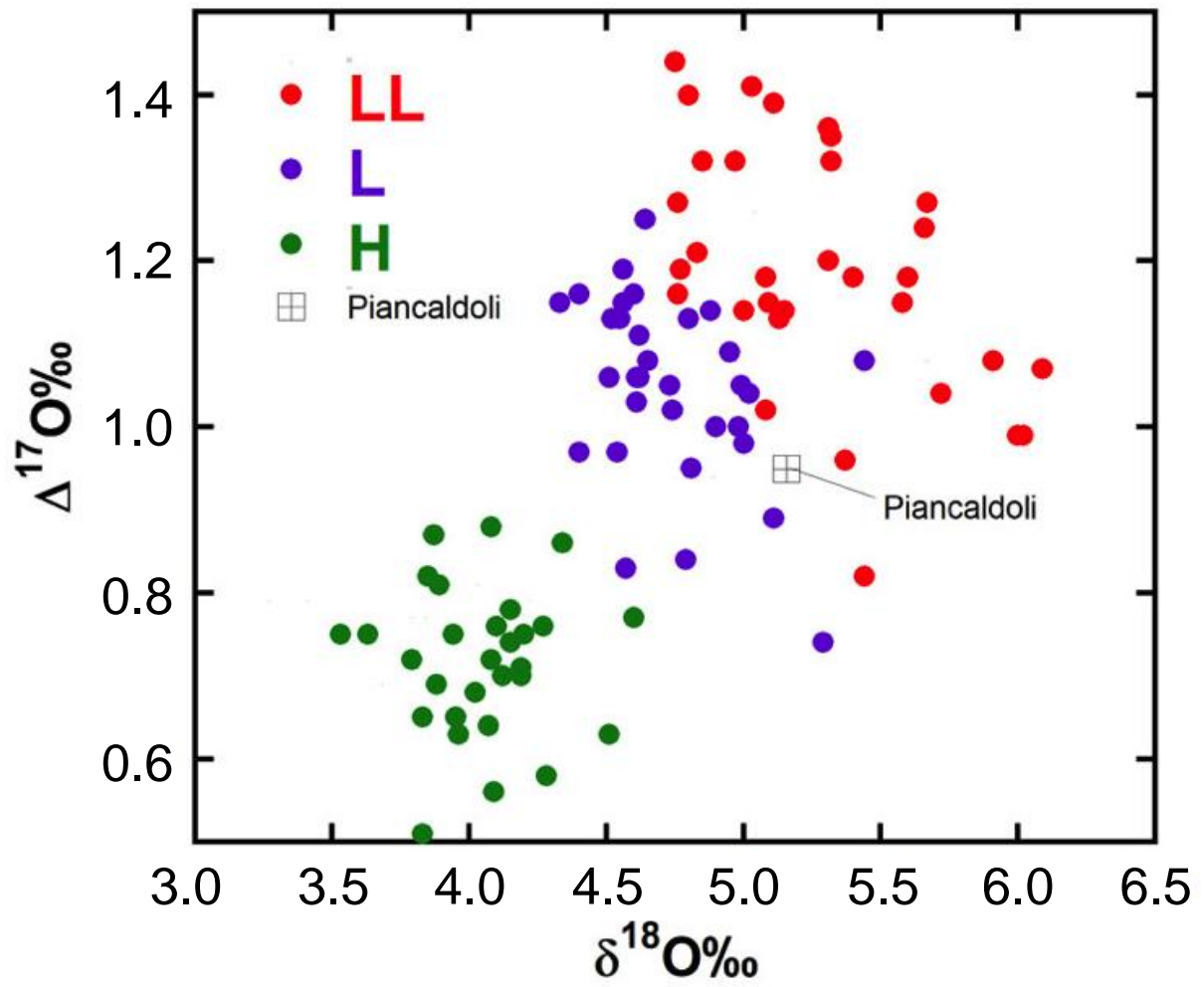
694



695

696

Fig. 11



697

698

Fig. 12

699

700

701

702

703

704

705

706

707